

A Practical Computational Hemolysis Model Incorporating Biophysical Properties of the Red Blood Cell Membrane

Nico Dirkes^{1*} and Marek Behr¹

¹Chair for Computational Analysis of Technical Systems, RWTH Aachen University, Schinkelstr. 2, Aachen, 52062, Germany.

*Corresponding author(s). E-mail(s): dirkes@aices.rwth-aachen.de;

Abstract

Purpose: Hemolysis is a key issue in the design of blood-handling medical devices. Computational prediction of this phenomenon is challenging due to the complex multiscale nature of blood. As a result, conventional approaches often fail to predict hemolysis accurately, commonly showing deviations of multiple orders of magnitude compared to experimental data. More accurate models are typically computationally expensive and thus impractical for real-world applications. This work aims to fill this gap by presenting accurate yet simple and efficient computational hemolysis models.

Methods: Hemolysis modeling relies on two key components: a red blood cell model and a hemoglobin release model. In this work, we compare three red blood cell models: a common stress-based model (Bludszuweit), a simple strain-based model based on the Kelvin-Voigt constitutive law, and a more complex tensor-based model (TTM). Further, we compare two hemoglobin release models: the widely used power-law approach and a biophysical pore formation model.

Results: We evaluate these models in two benchmark cases: the FDA blood pump and the FDA nozzle. In both benchmarks, the simple strain-based model combined with the pore formation model achieves absolute predictions of hemolysis within the standard deviation of experimental measurements. In contrast, stress-based power law models deviate by several orders of magnitude.

Conclusion: The strain-based pore modeling approach takes into account the biophysical properties of red blood cell membranes, in particular their viscoelastic deformation behavior and hemoglobin release through membrane pores. This leads to significantly improved hemolysis predictions in a framework that can easily be integrated into common CFD workflows.

Keywords: hemolysis, computational hemodynamics, red blood cell, blood damage

1 Introduction

Computational analysis has become an indispensable tool in the design process of blood-handling medical devices, such as ventricular assist devices, as it allows to predict device performance prior to manufacturing and testing. Two particular areas of interest are hydraulic performance, quantifying the pressure head and flow rate, and hematologic performance, quantifying the damage to blood components, such as red blood cells (RBCs). The hematologic performance consists of multiple aspects, among which *hemolysis*, i.e., flow-induced RBC damage, is of particular clinical relevance [1]. In hemolysis, fluid stresses distort the RBC, which can lead to membrane poration and ultimately rupture. As a result, the hemoglobin contained within the RBC leaks out into blood plasma, which can lead to severe complications, such as renal failure, bleeding and thrombosis [2–4]. While computational fluid dynamics (CFD) has matured to a reliable tool for predicting hydraulic performance, the accurate prediction of hemolysis remains challenging. In a recent interlaboratory study [5], hydraulic predictions were generally within a range of $\pm 20\%$ of experimental values, whereas hemolysis predictions varied by multiple orders of magnitude. This highlights the lack of reliable hemolysis models and calls for the development of improved approaches.

The reason hemolysis prediction is challenging lies in the complex multiscale nature of the problem. Hemolysis occurs on the scale of individual RBCs, which have a diameter of approximately $8\text{ }\mu\text{m}$. In contrast, blood-handling medical devices have characteristic dimensions on the order of centimeters, i.e., four orders of magnitude larger. Plenty of detailed numerical methods exist to resolve the shape of individual RBCs [6–10]. These methods can accurately capture the biophysical properties of the RBC membrane and support insights into the underlying mechanisms of hemolysis. However, their computational cost limits the number of RBCs that can be simulated. As a result, these methods typically track only a small fraction of all RBCs flowing through a device, evaluating hemolysis along their individual trajectories. Such Lagrangian approaches have two main drawbacks. First, it is unclear how to select a representative sample of RBCs to achieve accurate predictions. Second, the selected RBCs may not penetrate all relevant regions of the flow domain, such as small gap flows, boundary layers, and recirculation zones. Since these regions are most critical for hemolysis, resolving them accurately is essential for a model's utility in device design. For these reasons, such Lagrangian hemolysis models are not well suited to support the design process of blood-handling medical devices.

Eulerian models, on the other hand, treat blood as a continuum and describe the average behavior of RBCs at each point in space and time. This gives a spatially resolved field for RBC deformation, allowing for easy identification of critical regions inside the domain. However, developing accurate Eulerian hemolysis models is challenging. The models need to incorporate microscale behavior of RBCs into effective constitutive equations on the macroscale. In this work, we will focus on modeling two important biophysical properties of the RBC membrane: the viscoelastic deformation in response to fluid stress and the formation of pores as physical mechanism for hemoglobin release.

The viscoelastic nature of the RBC membrane has been documented extensively in literature [11–14]. Conventional hemolysis models, so-called *stress-based* models,

often neglect this property and assume that RBCs deform instantaneously to their steady state when encountering fluid stress. However, the importance of incorporating viscoelastic effects into hemolysis models has recently been highlighted again experimentally [15]. So-called *strain-based* hemolysis models incorporate viscoelastic RBC deformation models to account for the characteristic response of RBCs to fluid stress. The simplest form of a viscoelastic model is the scalar Kelvin-Voigt (KV) model, which consists of a spring and a dashpot in parallel. It does not explicitly resolve the membrane structure but provides a scalar measure of its deformation over time. It captures both the elastic and viscous response of the membrane to fluid stress. This model has first been suggested in the context of RBC mechanics by Katchalsky et al. [13]. Afterwards, Rand [14] extended the model by an additional spring and dashpot in series to capture the flowing behavior of RBCs. More recently, this approach has been extended to directly model the plasma-free hemoglobin [16–18]. However, these extended forms of the KV model are generally only valid for specific flow conditions, such as constant shear rates [16] or Poiseuille flow [17]. Extensions to more general three-dimensional flow fields have been attempted with mixed success [19–21]. In addition, these models are scalar in nature and do not consider the effect of three-dimensional stress states on RBC deformation. For this reason, we will focus on two particular models: the KV model and tank-treading model (TTM) [22]. While the KV model resolves viscoelastic deformation in a scalar manner, the TTM approximates RBCs as three-dimensional ellipsoids and captures their orientation in space. Thus, it accounts for the effect of three-dimensional stress states on RBC deformation. In particular, this can account for the difference between shear and extensional stress [23, 24]. The comparison of these two models will allow us to assess the importance of resolving three-dimensional stress states for hemolysis prediction.

The formation of pores in the RBC membrane under excessive membrane strain causes hemoglobin release through diffusion and advection. This mechanism is assumed to be the primary mechanism for sublethal hemolysis [25]. In contrast, lethal hemolysis occurs when the membrane ruptures entirely, releasing all hemoglobin contained within the RBC at once. While there have been attempts to combine models for sublethal and lethal hemolysis [26, 27], the additional complexity was overall deemed to be of limited benefit. Thus, we will focus on modeling sublethal hemolysis only. Historically, hemoglobin release has often been modeled using empirical power-law correlations that relate fluid stress and exposure time to hemolysis [28, 29]. However, such models are purely empirical and do not incorporate the underlying biophysical mechanisms of hemolysis. In contrast, pore formation models describe hemoglobin release based on the number and size of pores formed in the RBC membrane as a function of membrane strain. Vitale et al. [30] presented a first biophysical model for pore formation and hemoglobin release, assuming a uniform pore distribution on the membrane. The model is applicable in both Eulerian and Lagrangian frameworks. Afterwards, Sohrabi and Liu [31] developed a more complex model with non-uniform pore distribution for more general shape distortions. Due to the increased complexity, the model is only applicable in Lagrangian formulation. We will employ the simpler model by Vitale et al. [30] in the present work, as it is more suitable for our Eulerian approach, and has been shown to achieve satisfactory results in previous studies [32].

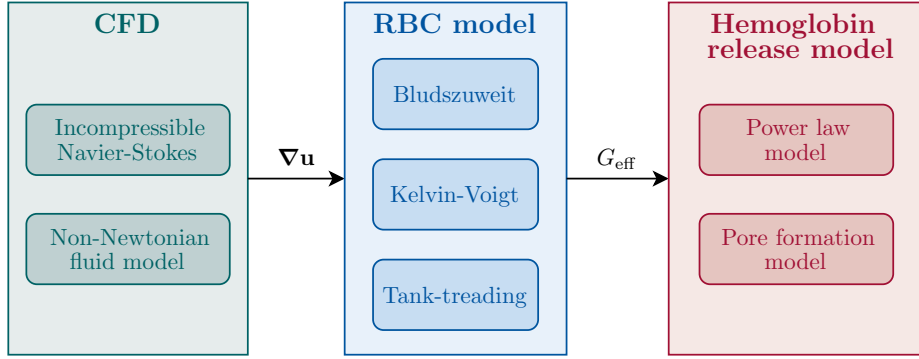


Fig. 1: Hemolysis model components.

The novelty in our approach thus lies in the combination of the aforementioned aspects: We aim to find a simple macroscopic Eulerian hemolysis model that captures viscoelastic effects and pore formation. This combination results in a computationally efficient hemolysis model that incorporates important biophysical properties of the RBC membrane and provides spatially resolved fields to aid the design process of medical devices. It should be easy to implement in existing CFD solvers, and be applicable to general three-dimensional flow fields for large-scale simulations of blood-handling medical devices. We further aim to validate our model against experimental data for relevant benchmark problems to prove its accuracy and reliability. For comparison, we evaluate different combinations of stress-based and strain-based approaches with empirical power law and pore-based hemoglobin release models, providing a comprehensive assessment of the different modeling choices.

This paper is structured as follows: In Section 2, we present the three fundamental components of our computational hemolysis framework, namely CFD, RBC model, and hemoglobin release model. We present different choices for each component and discuss their advantages and disadvantages. We show how we evaluate these models numerically. In Section 3, we present results for two benchmark problems defined by the U.S. Food and Drug Administration (FDA): a rotary blood pump and a nozzle. We evaluate different combinations of RBC models and hemoglobin release models and compare them to experimental data. In Section 4, we discuss the results and their implications for future research.

2 Methods

Hemolysis models generally consist of three components: CFD to determine the flow field, an RBC model to evaluate cell deformation, and a hemoglobin release model to quantify plasma-free hemoglobin. The overall workflow is illustrated in Fig. 1. This section outlines the different modeling choices for these components and the numerical methods we use to solve them.

2.1 Computational Fluid Dynamics

In this work, we model blood as an incompressible Newtonian fluid. The governing equations are the continuity equation and the Navier-Stokes equations:

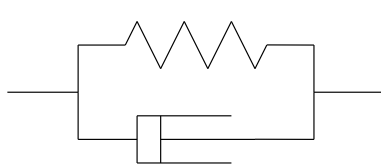
$$\nabla \cdot \mathbf{u} = 0, \\ \rho \left[\frac{\partial \mathbf{u}}{\partial t} + (\mathbf{u} \cdot \nabla) \mathbf{u} \right] = \mu \nabla \cdot \mathbf{E} - \nabla p, \quad \mathbf{E} = \frac{1}{2} \left((\nabla \mathbf{u}) + (\nabla \mathbf{u})^T \right),$$

Here, \mathbf{u} is the fluid velocity, p is the pressure, ρ is the density, μ is the dynamic viscosity, and \mathbf{E} is the rate of strain tensor. The Newtonian fluid assumption is commonly used in large vessels and at high shear rates [33]. More sophisticated fluid models exist to account for the non-Newtonian behavior of blood [7, 34, 35]. In this work, we will focus on the Newtonian assumption. However, all presented RBC and hemoglobin models may easily be combined with non-Newtonian fluid models. Independent of the employed fluid model, the CFD generally only needs to provide the velocity field $\mathbf{u}(\mathbf{x}, t)$ and the velocity gradient $\nabla \mathbf{u}(\mathbf{x}, t)$ to the RBC model.

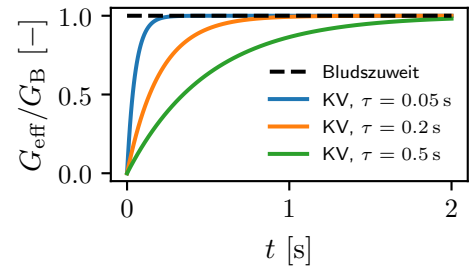
For viscoelastic models, the fluid stresses are typically split into a solvent and polymeric contribution. In that case, the solvent contribution is based on the rate of strain tensor \mathbf{E} , while the polymeric contribution is based on additional equations that model the underlying microstructure of the fluid on the macroscopic scale. The RBC models presented in the following section incorporate similar microstructural effects in a one-way coupling. The most direct approach to couple them to viscoelastic fluid models is thus to simply use the full velocity gradient $\nabla \mathbf{u}$ from a viscoelastic CFD simulation in the same one-way coupling. A more sophisticated approach is to directly integrate the RBC model into the viscoelastic fluid model, resulting in a two-way coupling. This is the subject of ongoing research.

2.2 Red Blood Cell Models

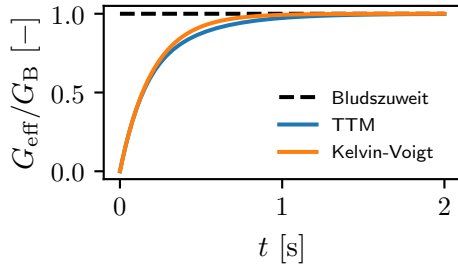
We consider three different RBC models to evaluate cell deformation in response to the flow field obtained from the CFD simulation: the Bludszuweit model, the tank-treading model (TTM), and the Kelvin-Voigt (KV) model. These models differ in complexity and the biophysical properties they account for. An overview of the differences between the models is given in Fig. 2. All models employ the concept of an *effective shear rate* G_{eff} to quantify cell deformation. This quantity represents the equivalent fluid shear rate that would lead to the same deformation at steady state under simple shear. The effective shear rate is then used in the hemoglobin release model to quantify hemolysis. We employ the effective shear rate instead of the effective shear stress $\sigma_{\text{eff}} = \mu G_{\text{eff}}$ in order to achieve independence from the fluid viscosity μ . In fact, a recent study [36] has found that hemolysis depends primarily on the shear rate rather than the shear stress.



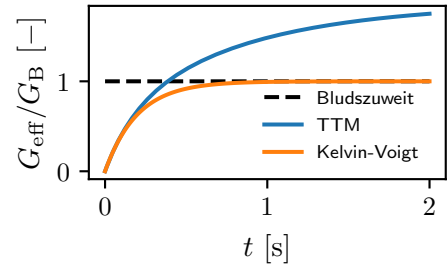
(a) Schematic of the KV model consisting of a spring and dashpot in parallel.



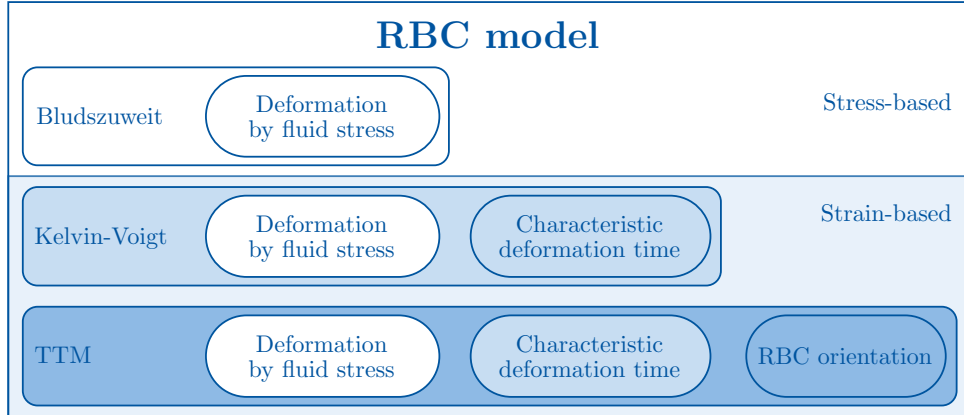
(b) Response of stress-based Bludszuweit model and strain-based KV model to a step increase in fluid shear rate G_B for different relaxation times τ .



(c) Response of RBC models to step increase in simple shear flow.



(d) Response of RBC models to step increase in extensional flow.



(e) Overview of effects taken into account by the three different RBC models.

Fig. 2: Illustration of the differences between the three types of RBC models employed in this work.

First, we define the Bludszuweit shear rate G_B in analogy to the representative stress proposed by Bludszuweit [37]:

$$G_B = \frac{2}{\sqrt{3}} \sqrt{E_{xx}^2 + E_{yy}^2 + E_{zz}^2 - E_{xx}E_{yy} - E_{yy}E_{zz} - E_{zz}E_{xx} + 3(E_{xy}^2 + E_{yz}^2 + E_{zx}^2)}. \quad (1)$$

This serves as a scalar measure of the three-dimensional rate of strain tensor \mathbf{E} . The *stress-based* approach consists of setting the effective shear rate G_{eff} equal to the Bludszuweit shear rate:

$$G_{\text{eff}} = G_B. \quad (2)$$

As Fig. 2b illustrates, this corresponds to an instantaneous elastic response of the RBC to fluid stress.

Next, we consider the *strain-based* modeling approach. Models in this category take into account the viscoelastic properties of the RBC membrane [11]. The viscoelastic response has been shown to be essential in modeling the effect of short-term stresses [15]. The simplest way to account for this is using a zero-dimensional KV model for a viscoelastic solid, namely a spring and dashpot in parallel. The spring governs the elastic response and limits the deformation under constant load. The dashpot governs the viscous response and introduces a time delay in the deformation. This scheme is illustrated in Fig. 2a. If the deformation of the RBC is expressed by the effective shear rate G_{eff} , the KV model results in the following transport equation:

$$\frac{DG_{\text{eff}}}{Dt} = F^{\text{KV}}(G_{\text{eff}}; \nabla \mathbf{u}) := \frac{1}{\tau}(G_B - G_{\text{eff}}), \quad (3)$$

where τ is the relaxation time of the material, which governs the timescale of the viscoelastic response to changes in fluid stress. The effect of this parameter is illustrated in Fig. 2b. The smaller the timescale τ , the faster the response to a sudden change in fluid stress. For $\tau \rightarrow 0$, the KV model tends to the Bludszuweit model (2), as the response becomes instantaneous. In that sense, it extends the purely elastic stress-based model by viscoelastic effects. In this work, we set $\tau = 200$ ms based on experimental data [38, 39].

Finally, we present the tank-treading model (TTM) [22]. It approximates red blood cells as ellipsoids. Each ellipsoid is described in terms of its semi-axes:

$$\boldsymbol{\Lambda} = \text{diag}(\lambda_1, \lambda_2, \lambda_3), \quad \mathbf{V} = [\mathbf{v}_1 \ \mathbf{v}_2 \ \mathbf{v}_3].$$

The length of the i -th semi-axis is given by $\sqrt{\lambda_i}$, and the normalized direction of the i -th semi-axis is given by the vector \mathbf{v}_i . The matrix \mathbf{V} thus describes the orientation of the ellipsoid in space. The model is written as a transport equation for $\boldsymbol{\Lambda}$:

$$\frac{D\boldsymbol{\Lambda}}{Dt} = \mathbf{F}^{\text{TTM}}(\boldsymbol{\Lambda}; \nabla \mathbf{u}), \quad F_i^{\text{TTM}}(\boldsymbol{\Lambda}; \nabla \mathbf{u}) = -f_1[\lambda_i - g(\boldsymbol{\Lambda})] + 2f_2\lambda_i E_{ii}^{\mathbf{V}}, \quad (4a)$$

$$\mathbf{E}^{\mathbf{V}} = \mathbf{V}^T \mathbf{E} \mathbf{V}, \quad \mathbf{V} = \begin{cases} \mathbf{V}_*(\nabla \mathbf{u}, \boldsymbol{\Lambda}), & \text{tank-treading,} \\ \mathbf{0}, & \text{tumbling.} \end{cases} \quad (4b)$$

We choose $f_1 = \frac{1}{\tau} = 5 \text{ s}^{-1}$ and $f_2 = 4.2298 \cdot 10^{-4}$ to match relaxation time and surface strain of experimental data, see [40]. Equation (4a) models the viscoelastic deformation of the RBC with the same relaxation time τ as the KV model. Equation (4b) models the orientation dynamics of the RBC, accounting for tank-treading and tumbling motions depending on the flow conditions $\nabla \mathbf{u}$ and deformation Λ . The orientation equation can be solved in an iterative algorithm. Assuming that $\lambda_1 > \lambda_2 > \lambda_3$, the effective shear rate in this model is computed from the deformation of the ellipsoid as

$$G_{\text{eff}} = \frac{2Df_1}{(1 - D^2)f_2}, \quad D = \frac{\sqrt{\lambda_1} - \sqrt{\lambda_3}}{\sqrt{\lambda_1} + \sqrt{\lambda_3}}. \quad (4c)$$

The differences between the three models are illustrated in Figs. 2c and 2d. In simple shear flow, the TTM and KV model are practically identical, as both models predict viscoelastic response with a characteristic relaxation time of 200 ms. In extensional flow, however, the TTM predicts a significantly higher deformation. This is due to the alignment of the red blood cell axes with the principal axes of fluid stress, and has been observed experimentally [24]. For more details on the incorporation of this effect in the TTM, see also [23]. An overview of the three presented RBC models is given in Fig. 2e.

Having introduced the defining features of the three RBC models employed in this work, we now define quantities to compare them systematically. First, we note that the TTM requires a logarithmic formulation for stability in complex flows, in analogy to other tensor-based models [22, 41]:

$$\frac{D\hat{\Lambda}}{Dt} = \mathbf{F}^{\text{TTLM}}(\hat{\Lambda}; \nabla \mathbf{u}). \quad (5)$$

We call this the logarithmic tank-treading model (TTLM). We analogously write the KV model in logarithmic form for consistency:

$$\frac{D\hat{G}_{\text{eff}}}{Dt} = F^{\text{KVL}}(\hat{G}_{\text{eff}}; \nabla \mathbf{u}) := G_{\text{B}}/G_{\text{eff}} - 1, \quad G_{\text{eff}} = e^{\hat{G}_{\text{eff}}/\tau}. \quad (6)$$

We call this the logarithmic Kelvin-Voigt (KVL) model. In order to evaluate the effect of the logarithmic formulation, we define the relative difference in effective shear rates predicted by the KVL and the original KV model:

$$\delta_G^{\text{KV;KVL}} = \frac{G_{\text{eff}}^{\text{KV}} - G_{\text{eff}}^{\text{KVL}}}{G_{\text{eff}}^{\text{KVL}}}. \quad (7)$$

The KVL further serves as a basis for comparison with the TTLM, as both models employ a logarithmic formulation. We compute the relative difference in effective shear rates predicted by the two models:

$$\delta_G^{\text{KVL;TTLM}} = \frac{G_{\text{eff}}^{\text{KVL}} - G_{\text{eff}}^{\text{TTLM}}}{G_{\text{eff}}^{\text{TTLM}}}. \quad (8)$$

To further analyze the effect of the three-dimensional fluid stress and orientation, we define a shear-only version of the TTLM. This version reduces the three-dimensional velocity gradient to a simple shear flow, using the Bludszuweit shear rate (1):

$$\frac{D\Lambda^s}{Dt} = \mathbf{F}^{\text{TTLM}}(\Lambda^s; \nabla \mathbf{u}^s), \quad \nabla \mathbf{u}^s := \begin{pmatrix} 0 & G_B(\nabla \mathbf{u}) & 0 \\ 0 & 0 & 0 \\ 0 & 0 & 0 \end{pmatrix}. \quad (9)$$

Here, $\nabla \mathbf{u}^s$ imitates the velocity gradient in simple shear flow of intensity G_B . We then compute the effective shear rate G_{eff}^s from the deformation Λ^s of this shear-only model as in Eq. (4c). Overall, this version of the TTLM is equivalent to the KVL model, in that it considers only viscoelastic deformation through the magnitude of G_B , without any three-dimensional effects. The main difference is that this formulation allows us to compare more directly to the full TTLM, since it has the same equation structure in Λ . We thus employ this model to compute the relative differences in the largest eigenvalue and in the respective source term F_1 :

$$\delta_\Lambda = \frac{\lambda_1 - \lambda_1^s}{\lambda_1^s}, \quad \delta_F = \frac{F_1^{\text{TTLM}}(\Lambda; \nabla \mathbf{u}) - F_1^{\text{TTLM}}(\Lambda^s; \nabla \mathbf{u}^s)}{F_1^{\text{TTLM}}(\Lambda^s; \nabla \mathbf{u}^s)}. \quad (10)$$

On the one hand, δ_Λ quantifies the influence of the three-dimensional RBC orientation on the predicted *deformation*. On the other hand, δ_F quantifies the influence of 3D RBC orientation on the predicted *rate of deformation*.

2.3 Hemoglobin Release Models

Next, we present two choices for models to quantify hemoglobin release from damaged RBCs. Both models rely on the effective shear rate G_{eff} computed from the RBC models in Section 2.2, and compute the local index of hemolysis IH as a measure of increase in plasma-free hemoglobin concentration Hb :

$$IH(\mathbf{x}, t) = \frac{\text{Hb}(\mathbf{x}, t) - \text{Hb}_0}{\text{Hb}_0}.$$

To compare with experimental data, we report the modified index of hemolysis MIH as a global quantity by integrating IH over the outlet of the device Γ_{out} :

$$MIH = \frac{10^6}{Q} \int_{\Gamma_{\text{out}}} IH(\mathbf{x}, t) \mathbf{u}(\mathbf{x}, t) \cdot \mathbf{n} dA, \quad Q = \int_{\Gamma_{\text{out}}} \mathbf{u}(\mathbf{x}, t) \cdot \mathbf{n} dA. \quad (11)$$

First, we present the widely used power law model, originally proposed by Giersiepen et al. [28]:

$$IH = A \sigma_{\text{eff}}^\alpha t^\beta, \quad \sigma_{\text{eff}} = \mu G_{\text{eff}}. \quad (12)$$

It relates the index of hemolysis IH to the effective fluid stress σ_{eff} and the exposure time t . The parameters A , α , and β are fitted to experimental data. In the form of Eq. (12), the model is only valid for constant effective shear rates. To model varying

RBC Model	Species	A	α	β	Correlation coefficient (R)
stress-based	ovine	1.228×10^{-7}	1.9918	0.6606	0.8445
	human	3.458×10^{-8}	2.0639	0.2777	0.6821
	porcine	6.701×10^{-6}	1.0981	0.2778	0.8634
	bovine	9.772×10^{-7}	1.4445	0.2076	0.7162
strain-based	ovine	3.100×10^{-6}	1.4284	0.1511	0.8390
	human	5.339×10^{-5}	0.7258	0.1000	0.6903
	porcine	1.334×10^{-5}	1.0277	0.2407	0.8780
	bovine	2.982×10^{-5}	0.8799	0.2109	0.7592

Table 1: Power law parameters for different species and RBC models, fitted to experimental data of Ding et al. [29].

shear rates, there are various strategies, see [42]. We use the raw hemolysis data from Ding et al. [29] to fit the parameters for four different species: human, ovine, porcine, and bovine. For the stress-based model (2), we directly use the parameters reported by Ding et al. [29]. For the strain-based models (3) and (4), we use the analytical solution of the KV model for constant fluid shear rates to compute the effective shear rate over time. We then employ the linearized form of the power law model to compute the index of hemolysis:

$$\ell_{IH} = IH^{\frac{1}{\beta}}, \quad \frac{D\ell_{IH}}{Dt} = A^{\frac{1}{\beta}} \sigma_{\text{eff}}^{\frac{\alpha}{\beta}}(t), \quad \sigma_{\text{eff}}(t) = \mu G_{\text{eff}}(t), \quad G_{\text{eff}}(t) = G_B \left(1 - e^{-t/\tau}\right).$$

The parameters (A, α, β) for the strain-based power law are determined by fitting the results to the raw experimental data of Ding et al. [29]. For this purpose, the ordinary differential equation (ODE) for ℓ_{IH} is integrated numerically with Python using `scipy.integrate.quad`. The parameter fitting is performed using `scipy.optimize.curve_fit`. The resulting parameters are summarized in Table 1. In analogy to Ding et al. [29], we report the correlation coefficient R as a measure of goodness of fit.

There are a number of drawbacks to the power law model. First, the model is purely empirical and does not account for the underlying biophysical mechanisms of hemolysis. Second, it has been shown that many choices of parameters (A, α, β) can fit the same experimental data almost equally well, leading to large variations in the determined hemolysis parameters [43]. Third, the extension to non-constant fluid stress histories is not always valid. In particular for rapidly changing shear rates, the linearization can induce significant errors [44]. However, the approach is frequently used in practice due to its simplicity [15, 21, 45, 46]. Extensions have been proposed to include threshold and saturation effects [21].

Second, we present the pore formation model proposed by Vitale et al. [30]. Compared to the original model, we employ a simplified form:

$$\frac{DIH}{Dt} = h \sigma_B^k A_p(G_{\text{eff}}), \quad \sigma_B = \mu G_B. \quad (13a)$$

RBC Model	Species	h	k	Correlation coefficient (R)
stress-based	ovine	1.816×10^{-7}	1.5399	0.8281
	human	1.157×10^{-6}	1.0309	0.6218
	porcine	8.941×10^{-7}	1.1165	0.8811
	bovine	2.552×10^{-6}	0.9289	0.7657
strain-based	ovine	3.292×10^{-7}	1.4424	0.8203
	human	2.187×10^{-6}	0.9271	0.6064
	porcine	1.556×10^{-6}	1.0268	0.8741
	bovine	4.386×10^{-6}	0.8411	0.7561

Table 2: Pore formation parameters for different species and RBC models, fitted to experimental data of Ding et al. [29].

The model relates hemoglobin release to the formation of pores in the membrane. Compared to the original model, the factor $1/V_{\text{RBC}}$ has been absorbed into the parameter h , and the saturation term is dropped assuming $IH \ll 1$. Furthermore, we use the Bludszuweit stress σ_B instead of the Bludszuweit shear rate G_B for analogy to the power law model Eq. (12). This also enables a more direct fit of the model to experimental data, which is commonly reported in terms of fluid stress. The pore area A_p is a function of the effective shear rate G_{eff} , which is computed from the RBC models in Section 2.2. For easier evaluation, we derive a polynomial fit, see Appendix A:

$$A_p(G_{\text{eff}}) = \begin{cases} 0, & G_{\text{eff}} < G_1, \\ P_5\left(\frac{G_{\text{eff}}}{G_2}\right), & G_1 \leq G_{\text{eff}} < G_2, \\ P_5(1), & G_{\text{eff}} \geq G_2, \end{cases} \quad (13b)$$

$$P_5(x) = -13.41x^5 + 37.31x^4 - 48.91x^3 + 32.39x^2 + 0.63x - 0.16.$$

Here, $G_1 = 3750 \text{ s}^{-1}$ and $G_2 = 42000 \text{ s}^{-1}$ are threshold shear rates for pore formation and lethal hemolysis, respectively. The parameters h and k are again fitted to the experimental data of Ding et al. [29]. The effective shear rate G_{eff} is computed from either the stress-based model (2) or the strain-based model (3). For the strain-based model, we again use the analytical solution of the KV model for constant fluid shear rates to compute the effective shear rate over time. The resulting parameters are summarized in Table 2.

In contrast to the power law model, the pore formation model is based on biophysical considerations [30]. Its native differential formulation in Eq. (13a) makes it suitable for varying shear rates without further assumptions. However, it still relies on experimental data to fit its parameters.

2.4 Numerical Method

Having discussed the underlying model equations for the CFD, RBC, and hemoglobin release models, we now present how we solve these equations. We describe boundary

conditions and initial conditions first and then detail the numerical discretization and solution methods.

For the CFD, we impose the velocity at the inlet Γ_{in} and we set a no-slip boundary condition at all walls Γ_{wall} . At the outlet, we prescribe a zero-traction condition. As initial condition, we set zero velocity throughout the domain.

For the strain-based RBC models, we first note that Equations (3), (5), (6) and (9) can each be written in the following general form:

$$\frac{D\phi}{Dt} = \mathbf{F}(\phi, \nabla \mathbf{u}), \quad (14)$$

for a quantity of interest ϕ and right-hand side \mathbf{F} depending on the specific model. There are two fundamentally different interpretations of this equation: the Lagrangian and Eulerian description.

The Lagrangian description relies on tracking individual RBCs and evaluating the model along each trajectory. For a more detailed discussion of this approach, see [22, 42]. All models discussed here are available in Lagrangian form in the open-source code HemTracer (<https://github.com/nicodirkes/hemtracer>).

In this work, we will focus on the Eulerian description. This description employs a continuum approach, identifying the quantity of interest as a field $\phi(\mathbf{x}, t)$ over the entire domain. The general equation (14) then becomes a partial differential equation (PDE) in the form of an advection equation:

$$\frac{D\phi}{Dt} = \frac{\partial \phi}{\partial t} + (\mathbf{u} \cdot \nabla) \phi = \mathbf{F}(\phi, \nabla \mathbf{u}),$$

with a source term \mathbf{F} . For the RBC models, we prescribe undeformed cells as initial condition and steady deformation at the inlet as boundary condition. Concretely, the KV model (3) becomes:

$$\begin{aligned} \frac{\partial G_{\text{eff}}}{\partial t} + (\mathbf{u} \cdot \nabla) G_{\text{eff}} &= \frac{1}{\tau} [G_{\text{B}} - G_{\text{eff}}], & \mathbf{x} \in \Omega, \quad t > 0, \\ G_{\text{eff}} &= 0, & \mathbf{x} \in \Omega, \quad t = 0, \\ G_{\text{eff}} &= G_{\text{B}}, & \mathbf{x} \in \Gamma_{\text{in}}, \quad t > 0. \end{aligned}$$

The KVL model (6) is transformed accordingly. Due to the singularity at $G_{\text{eff}} = 0$, we set a small offset in the initial condition:

$$\begin{aligned} \frac{\partial \hat{G}_{\text{eff}}}{\partial t} + (\mathbf{u} \cdot \nabla) \hat{G}_{\text{eff}} &= G_{\text{B}} e^{-\hat{G}_{\text{eff}}/\tau} - 1, & \mathbf{x} \in \Omega, \quad t > 0, \\ \hat{G}_{\text{eff}} &= -2, & \mathbf{x} \in \Omega, \quad t = 0, \\ \hat{G}_{\text{eff}} &= \tau e^{G_{\text{B}}}, & \mathbf{x} \in \Gamma_{\text{in}}, \quad t > 0. \end{aligned}$$

For the TTLM (5), we employ the analytical steady state solution (A13) to compute the transformed eigenvalues at the inlet:

$$\begin{aligned} \frac{\partial \hat{\lambda}_i}{\partial t} + (\mathbf{u} \cdot \nabla) \hat{\lambda}_i &= F_i^{\text{TTLM}}(\hat{\Lambda}; \nabla \mathbf{u}), \quad \mathbf{x} \in \Omega, \quad t > 0, \quad i \in \{1, 3\}, \\ \hat{\lambda}_i(\mathbf{x}, 0) &= -2, \quad \mathbf{x} \in \Omega, \quad t = 0, \\ \hat{\lambda}_i(\mathbf{x}, t) &= \hat{\lambda}_i^{\text{steady}}(G_B), \quad \mathbf{x} \in \Gamma_{\text{in}}, \quad t > 0, \\ \lambda_1 &= 1 + e^{\hat{\lambda}_1}, \quad \lambda_2 = \frac{1}{\lambda_1 \lambda_3}, \quad \lambda_3 = \frac{1}{1 + e^{\hat{\lambda}_3}}. \end{aligned}$$

The formulation for the shear-only TTLM (9) is analogous.

For the hemoglobin release models, we employ the volume integral approach proposed by Garon and Farinas [47]. This approach assumes zero hemolysis at the inlet and exploits the divergence theorem. This way, the boundary integral in Eq. (11) can be computed directly from a volume integral of the hemoglobin release source term over the domain Ω , avoiding the need to solve an additional transport equation for IH . Furthermore, it allows for more instantaneous feedback on global hemolysis in unsteady simulations, which otherwise require propagating IH concentration up to the outlet. For the power law model (12), this volume integral becomes:

$$MIH(t) = \frac{10^6}{Q} \left[\int_{\Omega} A^{1/\beta} \sigma_{\text{eff}}^{\alpha/\beta}(\mathbf{x}, t) d\mathbf{x} \right]^{\beta}, \quad \sigma_{\text{eff}}(\mathbf{x}, t) = \mu G_{\text{eff}}(\mathbf{x}, t),$$

For the pore formation model (13), the volume integral becomes:

$$MIH(t) = \frac{10^6}{Q} \int_{\Omega} h \sigma_B^k(\mathbf{x}, t) A_p(G_{\text{eff}}(\mathbf{x}, t)) d\mathbf{x}, \quad \sigma_B(\mathbf{x}, t) = \mu G_B(\mathbf{x}, t),$$

with the piecewise polynomial A_p from Eq. (13b). For unsteady simulations, we average $MIH(t)$ over time to obtain a global value MIH .

All problems are solved using our in-house multiphysics stabilized finite element code [22]. We use piecewise linear FEM as space discretization and an implicit second-order BDF2 time-stepping scheme. We treat rotating machinery using the multiple reference frame (MRF) approach [48]. We employ variational multiscale (VMS) stabilization, which separates the solution into resolved and unresolved scales. The application of this method to unsteady turbulent flows can be interpreted as a form of large eddy simulation (LES) [49].

3 Results

We present the application of these models to two benchmark cases defined by the FDA: the FDA blood pump and the FDA nozzle.

3.1 FDA Blood Pump

CFD simulations of the FDA blood pump have previously been performed by Haßler et al. [32]. In the same work, the results have been validated against experimental particle image velocimetry (PIV) data. We therefore use the same computational mesh and the same time-averaged flow field for hemolysis modeling in the present work.

First, the flow field is used to determine G_{eff} using the three RBC models presented in Section 2.2. We use a logarithmic scale due to the large range of effective shear rates present in the pump. The stress-based model in Fig. 3a predicts the highest effective shear rates overall, with peak values exceeding $95\,000\,\text{s}^{-1}$ close to the walls and to the impeller blades. In comparison, the strain-based models predict lower effective shear rates at the wall, with maximum values of approximately $15\,000\,\text{s}^{-1}$. In the region in between the impeller blades, the strain-based models predict higher effective shear rates than the stress-based model due to the effect of the viscoelastic membrane relaxation. Qualitatively, the effective shear rates predicted by the three strain-based models from Eqs. (3), (5) and (6) are very similar. For this reason, we only show the effective shear rates from the regular KV model in Fig. 3b and the relative differences between the models in Figs. 3c and 3d. Quantitatively, the predictions from the regular KV model in Fig. 3b are between 50% and 100% higher than those from the KVL model in Fig. 3c. This suggests that numerical diffusion introduced by the logarithmic formulation significantly influences the effective shear rate predictions. In contrast, Fig. 3d shows that the two strain-based models in logarithmic formulation yield very similar results, with differences of less than 5%. Finally, the effect of RBC orientation is analyzed in Figs. 3e and 3f. The effective shear rates differ by less than 1% between the tank-treading model and its shear-only version. However, the effect on the source term is more pronounced, with differences of up to 100%, as shown in Fig. 3f.

Using the effective shear rates from the RBC models, we compute the MIH using the volume integral approach outlined in Section 2.4. In order to compare to the experimental data of Malinauskas et al. [50], which was obtained from porcine blood, we use the respective porcine parameters from Tables 1 and 2. The results for all six operating conditions of the pump are shown in Fig. 4. The stress-based Bludszuweit approach with the power law model overpredicts the experimental values by almost three orders of magnitude. Using the same hemoglobin model with the strain-based KV model instead leads to 50% smaller hemolysis predictions, but still significantly overpredicts the experimental values. The combination of the Bludszuweit RBC model with the pore formation model yields lower hemolysis predictions, overpredicting the experimental values by one and a half orders of magnitude. Only the combination of the strain-based KV model with the pore formation model leads to hemolysis predictions that are within the standard deviation of the experimental data for conditions 1, 3, 4, and 6. For conditions 2 and 5, the predictions slightly overestimate the experimental values. As Fig. 4b demonstrates, all strain-based RBC models yield similar results. The KVL and TTLM models predict slightly lower values than the regular KV model, as a result of the lower effective shear rates shown in Fig. 3c. The predictions of these two models are thus within a standard deviation for all conditions. Between the KVL and TTLM model, there are practically no differences in the predicted MIH values, confirming the observations made in Fig. 3d.

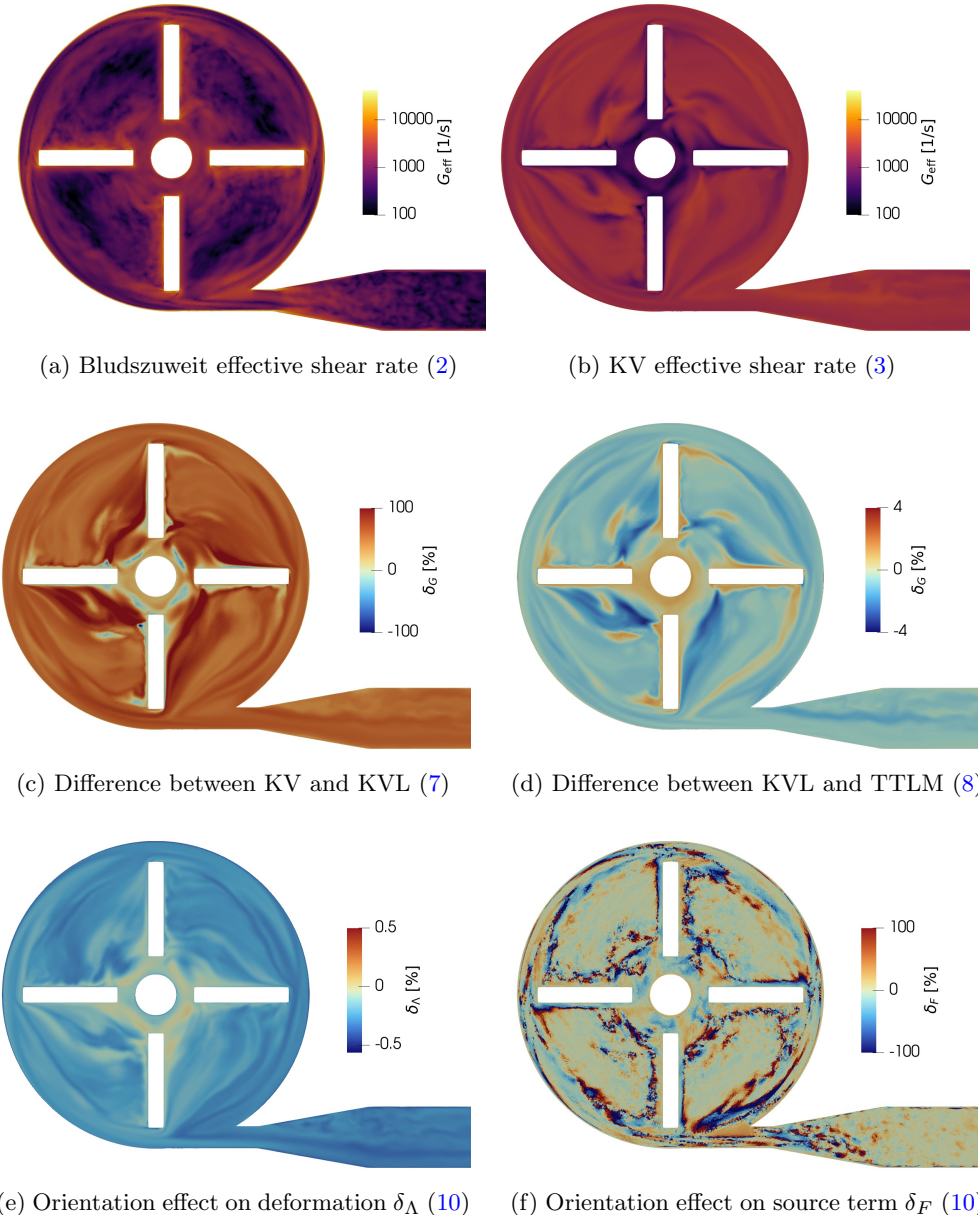
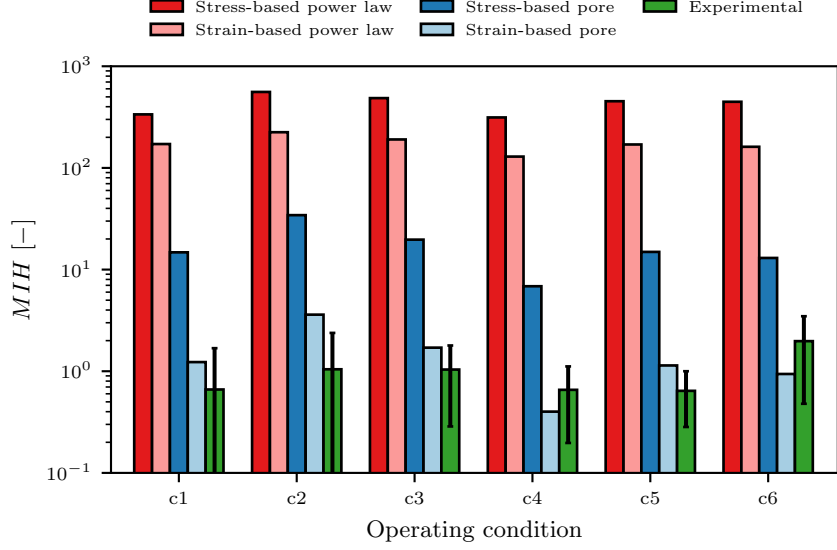
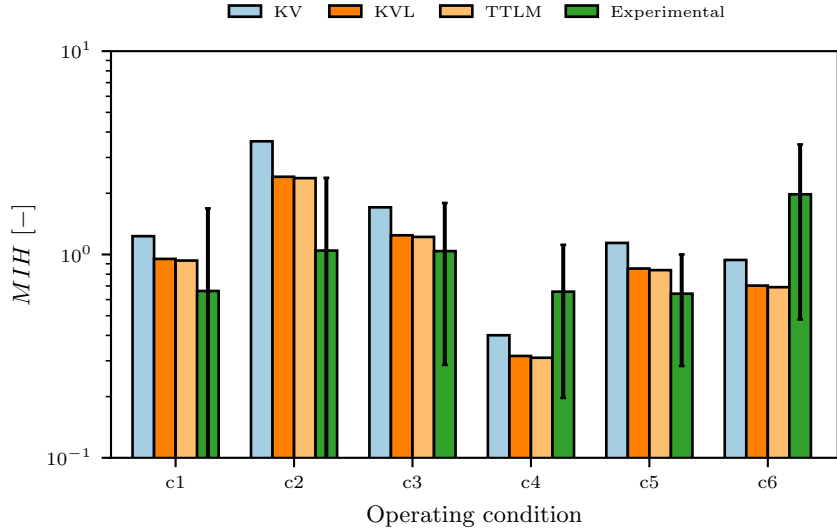


Fig. 3: RBC model results for the FDA blood pump at operating condition 4, evaluated on a plane intersecting the impeller at $z = 0.7$ cm.



(a) Stress-based (Bludszuweit) and strain-based (Kelvin-Voigt) RBC models with power law and pore models against experiments.



(b) Different forms of strain-based RBC models using the pore formation model for hemoglobin release.

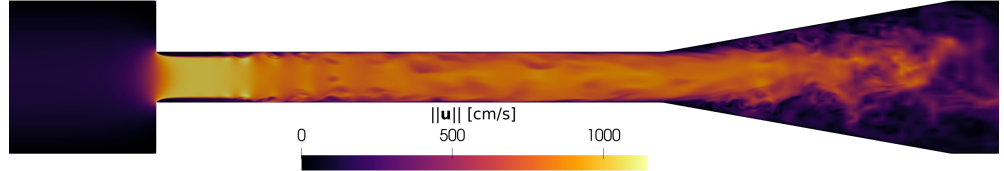
Fig. 4: Modified index of hemolysis (MIH) predictions for the FDA pump using different RBC models and different models for the hemoglobin release compared to experimental data from Malinauskas et al. [50].

3.2 FDA Nozzle

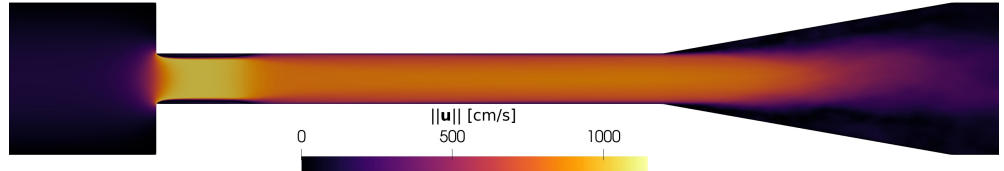
As a second benchmark case, we consider the FDA nozzle [51]. Similar to Mantegazza et al. [52], we focus on the sudden contraction orientation at a Reynolds number of $Re = 6500$, as this is the only configuration with both PIV data and hemolysis data. We employ a block-structured computational mesh with approximately 2.4 million hexahedral elements. In the throat region, the wall distance is approximately $12.5 \mu\text{m}$, which is within the Kolmogorov length scale of $20 \mu\text{m}$ reported by Mantegazza et al. [52]. We set a time step size of $1 \times 10^{-5} \text{ s}$ and simulate until a statistically stationary quasi-steady state is reached. From there, we compute the unsteady flow solution using the LES approach outlined in Section 2.4 for a total time of 20 ms. For the simulations, we employ a viscosity of $4.24 \times 10^{-3} \text{ Pas}$, a density of 1040 kg m^{-3} , and a volume flow rate of $6.77 \times 10^{-5} \text{ m}^3 \text{ s}^{-1}$. This corresponds to the conditions in the hemolysis experiments with bovine blood, as reported by Herbertson et al. [53].

In order to validate the flow solution with PIV data, we average the flow field in time over 20 ms. Since the PIV data was obtained by Hariharan et al. [51] with water at a higher flow rate, we non-dimensionalize the velocity by the mean inlet velocity \bar{u} . Similarly, we non-dimensionalize the pressure by the corresponding dynamic pressure $\rho\bar{u}^2/2$. Since the PIV measurements were performed at the same Reynolds number $Re = 6500$ as the simulations, dynamic scaling guarantees similarity. We compute the wall pressure by averaging the pressure values at the wall over the circumference at each axial position. Figure 5 shows the CFD results. As Fig. 5a visualizes, the flow in the throat region is highly unsteady, with vortices forming and shedding downstream of the sudden expansion. Figure 5b shows the corresponding time-averaged velocity field. This field is used as basis for the experimental validation. Figures 5c to 5f compare the CFD results to the data from Hariharan et al. [51]. The error bars indicate the standard deviation of the experiments. The axial direction z is defined in direction of the flow, with $z = 0 \text{ cm}$ at the sudden contraction. Overall, the velocity predictions along the centerline in Fig. 5c show very good agreement with the experimental data, with errors within the standard deviation. The predicted wall pressure in Fig. 5d is mostly within the experimental standard deviation, with some errors outside the standard deviation in the expansion region. The velocity profile in Fig. 5e at $z = 0.4 \text{ cm}$ is in the throat region immediately downstream of the contraction. The comparison shows less recirculation in the experiments compared to the RANS results, leading to deviations in the velocity profile close to the wall. Similar deviations have been observed by Mantegazza et al. [52]. Since the standard deviation is large in this region, there may be strong transient effects present in the experiments that are not fully captured by the time-averaged RANS solution. In contrast, the velocity profile in Fig. 5f at $z = 5.6 \text{ cm}$ in the diffuser region shows very good agreement with the experimental data throughout the profile.

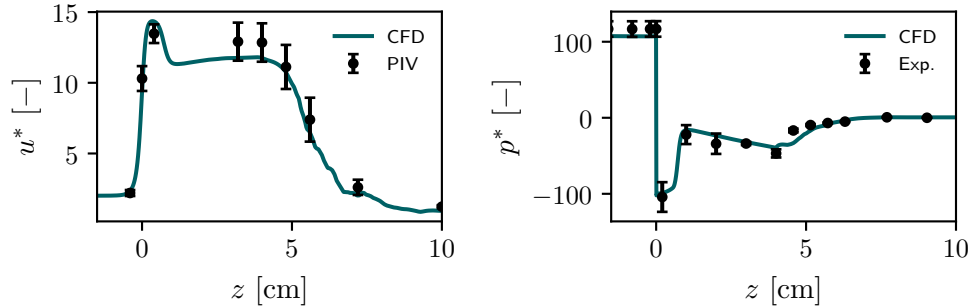
Next, we discuss the results of the various RBC models. We apply these models to the unsteady LES flow field. The fields visualized in Fig. 6 show the effective shear rates at one particular instant. The effective shear rates using the stress-based Bludszuweit model in Fig. 6a again exhibit the largest values of all models, with peak values in the nozzle up to $3 \times 10^5 \text{ s}^{-1}$. In comparison, the strain-based KV model in Fig. 6b predicts lower effective shear rates, with peak values in the nozzle of approximately



(a) Instantaneous velocity magnitude from LES solution.

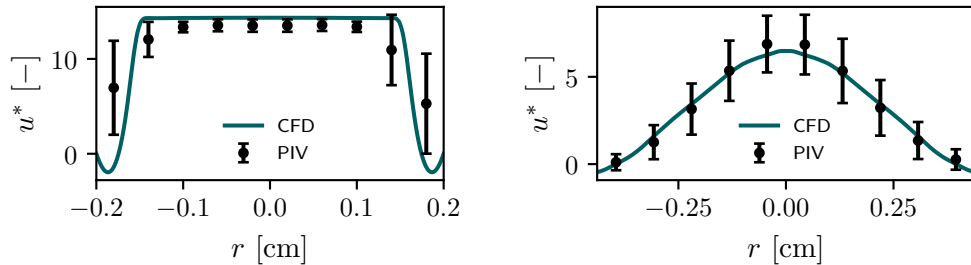


(b) Time-averaged velocity magnitude from Reynolds-averaged Navier-Stokes (RANS) solution.



(c) Non-dimensional RANS axial velocity along centerline compared to PIV data.

(d) Non-dimensional RANS wall pressure compared to experimental data.



(e) Non-dimensional RANS velocity profile at $z = 0.4$ cm (throat region) compared to PIV data.

(f) Non-dimensional RANS velocity profile at $z = 5.6$ cm (diffuser region) compared to PIV data.

Fig. 5: Flow field validation for the FDA nozzle in contraction orientation at $Re = 6500$ using data from Hariharan et al. [51].

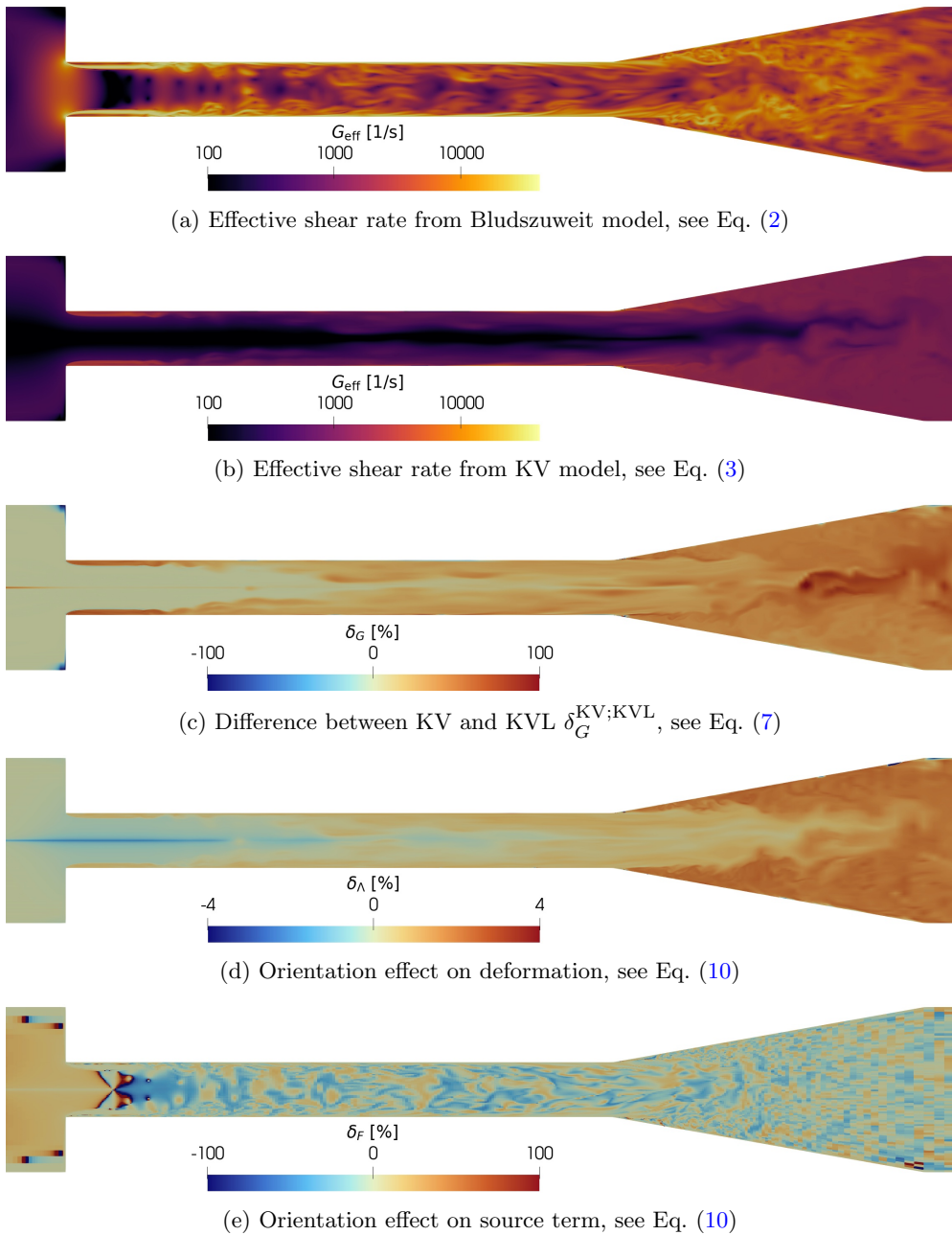
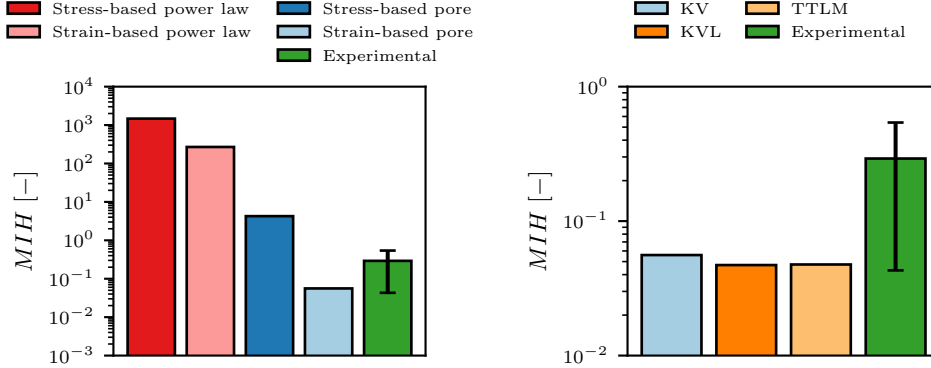


Fig. 6: RBC model results for the FDA nozzle in contraction configuration at $Re = 6500$, evaluated on a central axial plane.



(a) Stress-based (Bludszuweit) and strain-based (KV) RBC models with power law and pore models for hemoglobin release.

(b) Different versions of strain-based RBC models using the pore formation model for hemoglobin release.

Fig. 7: MIH predictions for the FDA nozzle in contraction configuration at $Re = 6500$, using different RBC models and hemoglobin release models, compared to experimental data from Herbertson et al. [53].

$1 \times 10^4 \text{ s}^{-1}$. Qualitatively, the KV model predicts a larger coherent region of elevated G_{eff} in the recirculation zone immediately downstream of the contraction. The relative difference between the KV and KVL models in Fig. 6c shows that the KV model again predicts up to 100% higher effective shear rates compared to the KVL model. The difference between the TTLM and KVL models is again much smaller and omitted here for brevity. Finally, the effect of the three-dimensional RBC orientation is shown in Figs. 6d and 6e. We observe the same trends as in the blood pump case in Figs. 3e and 3f: the effect on the source term is significant, but the resulting deformations are very similar.

Lastly, we compute the MIH using the volume integral approach from Section 2.4. Since the hemolysis experiments by Herbertson et al. [53] were performed with bovine blood, we use the respective bovine parameters from Tables 1 and 2. The results are shown in Fig. 7. Similar to the blood pump case in Fig. 4, the power law models overpredict the experimental values by three to four orders of magnitude. The pore formation models achieve better predictions overall. In particular, the strain-based RBC model in combination with the pore formation model yield predictions that are within the experimental standard deviation. The difference between the KV, KVL, and TTLM models is relatively small, with the KVL and TTLM models predicting slightly lower hemolysis than the regular KV model. In contrast, the stress-based Bludszuweit RBC in combination with the pore formation model overestimates the experimental values by approximately one order of magnitude. The power law model again leads to significant overpredictions between three and four orders of magnitude. Such overprediction is also observed in the results presented by Mantegazza et al. [52].

4 Discussion

Our results show that the strain-based pore formation model consistently outperforms the other combinations of RBC models and hemoglobin release models in both benchmark cases. It is able to accurately predict hemolysis over a wide range of operating conditions using a single set of model parameters fitted to literature data. This demonstrates the potential of the strain-based pore formation model as a universal tool for computational hemolysis prediction in complex blood flows. Its predictive capability is particularly notable given the simplicity of the model, which only requires solving a single linear advection equation for the effective shear rate and evaluating a volume integral to compute hemolysis. The model thus accounts for the underlying viscoelastic RBC deformation on a phenomenological level, without the need for explicit modeling of shape and orientation dynamics or interactions between individual cells.

Our results further confirm that Eulerian power law models tend to overpredict hemolysis, see also [5, 42, 44]. Since the original form of the power law (12) is written for constant stress in simple experimental conditions, any application to complex flows incurs various types of errors. For example, the linearization required for non-constant stress histories leads to numerical errors. In addition, the power law is purely empirical in nature. So while it may fit experimental data well in simple shear flow, there is no guarantee that it will generalize to more complex flow conditions. In contrast, the pore formation model is based on biophysical principles of membrane poration, making it more robust to variations in flow conditions. Its differential formulation (13a) allows it to naturally account for non-constant stress or strain histories without the need for linearization.

The current default approach for computational hemolysis prediction is the stress-based power law model (see the employed models in Ponnaluri et al. [5]). While the absolute hemolysis predictions of this approach are often inaccurate, it can still be useful for relative comparisons [52]. It is therefore often argued that the stress-based power law model is sufficient for distinguishing between iterative design variations of medical devices. However, as shown by Lommel et al. [15], stress-based models are not able to accurately capture the effect of short-term exposure to high shear stresses, which are common in medical devices. If the exposure time to these peaks or the magnitude of the peaks varies between different device designs, stress-based models may yield misleading results even for relative comparisons. In contrast, strain-based models are able to account for the viscoelastic response of RBCs to transient shear stresses, leading to more robust predictions in such scenarios. For these reasons, we find that strain-based models are generally preferable over stress-based models for computational hemolysis prediction.

On the different forms of strain-based RBC models, namely KV, KVL, and TTLM, our results indicate that the choice between them has only a minor impact on hemolysis predictions. In fact, we find larger variations between the logarithmic and regular formulation of the Kelvin-Voigt (KV) model than between KVL and TTLM. While the KV and KVL formulations are analytically equivalent, the piecewise linear finite element discretization of the logarithmic form introduces numerical diffusion, leading to lower effective shear rates and thus lower hemolysis predictions. With increasing mesh resolution, this difference is expected to decrease. The KVL and TTLM models,

on the other hand, differ mainly in their ability to account for the difference between shear and elongational flows. The difference between these models seems to be negligible for both benchmarks considered here. We employ the shear-only TTLM to analyze the reasons for this. We find that there is a significant influence of elongational versus shear stresses on the source terms. In accordance with our earlier analysis [23], there are significant coherent regions in the flow where the incorporation of these three-dimensional effects causes the source term to either increase or decrease substantially compared to the shear-only assumption. However, the effect on the resulting RBC deformation is small. We postulate that this is due to the short exposure times to either elevated or reduced source terms. Due to the characteristic deformation timescale of 200 ms, the RBCs do not have enough time to respond to these local variations before they are advected into a different flow region with different stress characteristics. Overall, these effects seem to cancel out, leading to similar predictions for both KVL and TTLM. There is thus little practical benefit in using the more complex TTLM over the KV or KVL models for typical medical device flows.

Next, we discuss the limitations of our modeling approach. First, the strain-based pore formation model does not explicitly resolve single cells or their microstructural behavior. In particular, it does not account for interactions between RBCs or detailed membrane mechanics. Instead, it models the average response of a population of RBCs to the local flow conditions using models informed by biophysical principles. While this phenomenological approach captures the values and trends of hemolysis well in the benchmark cases considered here, further validation against experimental data in real medical devices is needed to establish its generalizability. Second, these results do not include any coupling between RBC deformation and the surrounding fluid flow, assuming Newtonian fluid behavior. In reality, deformed RBCs affect the rheological properties of blood, which in turn affect the flow field. In a primitive approach, this could be accounted for by using shear-thinning viscosity models in the CFD simulation. A more rigorous approach would involve two-way coupling between RBC deformation and fluid flow. Third, our models assume constant hematocrit and do not account for variations in RBC concentration or aggregation effects, which can influence hemoglobin release. Incorporating these effects would require more complex multiphase flow models [34]. Fourth, the strain-based RBC models presented here only account for the stresses induced by the resolved flow field. In turbulent flows, additional stresses arise from velocity fluctuations at scales smaller than the grid resolution. For stress-based models, the inclusion of such stresses on the macroscopic scale has been studied using Reynolds shear stress [54] or energy dissipation rate [55]. For strain-based models, it is still an open question how incorporate turbulence effects, especially due to the large discrepancy between the timescales of turbulent fluctuations and RBC deformation.

In the future, we plan to extend our modeling approach in several directions. First, we intend to apply our workflow to real ventricular assist devices in order to further validate its predictive capability in practical applications. Second, we are working on incorporating two-way coupling between RBC deformation and fluid flow in the context of viscoelastic fluid models [35]. Third, we aim to perform uncertainty quantification for our hemolysis predictions and thus obtain estimates for the confidence intervals of our model outputs [56]. This will identify the magnitude of uncertainties

propagating from the experimental data used for model calibration [43]. Fourth, we want to obtain highly resolved turbulence data in order to study the effects of turbulent fluctuations on RBC deformation and hemolysis and develop suitable modeling approaches to account for these effects on a phenomenological level.

Overall, we have discovered a promising new approach for computational hemolysis prediction, consisting of a Kelvin-Voigt (KV)-based constitutive model for RBC deformation combined with a pore formation model for hemoglobin release. This approach consistently outperforms existing methods across two benchmark cases, and is simple to implement into existing CFD workflows. It can be applied to any converged CFD solution directly in the Eulerian frame, enabling detailed local analysis of RBC deformation as well as accurate global predictions of hemolysis. The improvements in accuracy are attributed to the biophysical basis of the KV model, which captures the viscoelastic deformation behavior of RBC membranes, as well as the pore formation model, which describes hemoglobin release through membrane pores.

Statements and Declarations

Competing Interests

The authors have no relevant financial or non-financial interests to disclose.

Funding

This work was funded by the Deutsche Forschungsgemeinschaft (DFG, German Research Foundation) through grant 333849990/GRK2379 (IRTG Modern Inverse Problems). The authors gratefully acknowledge the computing time provided to them at the NHR Centers NHR4CES at TU Darmstadt (project number p0020502) and RWTH Aachen University (project number p0024828). This is funded by the Federal Ministry of Research, Technology and Space, and the state governments participating on the basis of the resolutions of the GWK for national high performance computing at universities (www.nhr-verein.de/unsere-partner).

Acknowledgements

The authors would like to thank Dr. Zhongjun Jon Wu for providing us with the raw experimental data from Ding et al. [29] for the parameter fitting in Tables 1 and 2.

CRediT authorship contribution statement

Nico Dirkes: Conceptualization, Methodology, Software, Validation, Formal analysis, Investigation, Data Curation, Writing - Original Draft, Visualization, Software.
Marek Behr: Conceptualization, Writing - Review & Editing, Supervision, Project administration, Funding acquisition, Software.

Symbol	Value	Unit	Description
A_0	135	μm^2	Unstretched RBC surface area
σ'	3.2	mJ m^{-2}	Apparent hydrophobicity
ξ	8		Lipid tail rigidity
h_t	2.5	nm	Length of phospholipid tails
r_1	9.5×10^{-2}	nm	Radius of phospholipid heads
N_1	7.913×10^{-3}	μm^{-2}	Pore density at ε_1 , computed from Eq. (A4)
N_2	108.97	μm^{-2}	Pore density at ε_2 , computed from Eq. (A5)
A_2^*	5.5	%	Relative pore area at ε_2
ε_1	0.16	%	Threshold surface strain for pore formation
ε_2	6.0	%	Surface strain at lethal hemolysis
f_1	5.0	s^{-1}	Relaxation parameter in RBC model
f_2	4.2298×10^{-4}		Steady shear RBC deformation parameter
$G_{\text{eff}}^{(1)}$	3750	s^{-1}	Threshold effective shear rate, computed from Eq. (A16)
$G_{\text{eff}}^{(2)}$	42000	s^{-1}	Lethal effective shear rate, computed from Eq. (A16)
a_0	-0.159 299 74	μm^2	Polynomial fit coefficient, computed from Eq. (A18)
a_1	0.633 194 21	μm^2	Polynomial fit coefficient, computed from Eq. (A18)
a_2	32.392 089 45	μm^2	Polynomial fit coefficient, computed from Eq. (A18)
a_3	-48.914 873 32	μm^2	Polynomial fit coefficient, computed from Eq. (A18)
a_4	37.312 486 04	μm^2	Polynomial fit coefficient, computed from Eq. (A18)
a_5	-13.413 394 81	μm^2	Polynomial fit coefficient, computed from Eq. (A18)

Table A1: Parameters used for the evaluation of the pore area A_p . If not stated otherwise, the values are taken from Vitale et al. [30].

Appendix A Evaluation of the Pore Area

The pore model derived by Vitale et al. [30] defines the total pore area A_p per RBC as a function of the surface area strain ε of the RBC membrane:

$$\varepsilon = \frac{A_m - A_0}{A_0},$$

where A_m is the current membrane surface area and A_0 is the surface area of an undeformed RBC. This expression limits the pore model's applicability to RBC models that explicitly resolve the RBC shape, such as the TTM, see Eq. (4). In this section, we derive the pore area as a function of the effective shear rate G_{eff} instead. This allows for the application of the pore model to any RBC model that provides the effective shear rate. This section is split into two parts: First, we reiterate the model equations that relate the pore area to the surface area strain according to Vitale et al. [30]. Second, we describe how to compute the surface area strain for the models discussed in Section 2.2 and derive appropriate polynomial fits for easy evaluation. All parameters used in this section are summarized in Table A1.

We start by considering the normalized membrane energy, expressed as a fourth order polynomial of the pore radius r_0 and the pore density N :

$$\hat{W}_N(r_0) = AN^2r_0^4 - BNr_0^2 + CNr_0, \quad (\text{A1})$$

$$A(\varepsilon) = 2\pi^2[\sigma'\xi - \sigma'_0(\varepsilon)], \quad B = \sigma'_0(\varepsilon)\pi, \quad C = 2\pi\gamma(\varepsilon). \quad (\text{A2})$$

Note that the expression for A in Eq. (A2) differs from the one given by Vitale et al. [30]. With the original definition, we were not able to reproduce the values of N_1 and N_2 reported in their work. With the present definition, we obtain similar values (comp. Table A1). The surface tension of the intact membrane σ'_0 is computed as:

$$\sigma'_0(\varepsilon) = 2\sigma'\xi \left(1 - \frac{1}{(1+\varepsilon)^2}\right).$$

The pore edge energy γ is computed as:

$$\gamma(\varepsilon) = 2(h_t - \xi r_1 \varepsilon) \sigma'.$$

The critical pore density N_c at which pores start to form is given by:

$$N_c(\varepsilon) = \frac{8B(\varepsilon)^3}{27A(\varepsilon)C(\varepsilon)^2}. \quad (\text{A3})$$

As in [30], we compute N_1 from Eq. (A3) as

$$N_1 = N_c(\varepsilon_1), \quad (\text{A4})$$

and N_2 as:

$$r_2 = \frac{-\pi C(\varepsilon_2)}{4A(\varepsilon_2)A_2^* - 2\pi B(\varepsilon_2)}, \quad N_2 = \frac{2B(\varepsilon_2)r_2 - C(\varepsilon_2)}{4A(\varepsilon_2)r_2^3}. \quad (\text{A5})$$

The pore density is modeled as a function of the surface strain ε by an exponential interpolation between N_1 and N_2 :

$$N(\varepsilon) = N_1 \exp\left(\frac{\varepsilon - \varepsilon_1}{\varepsilon_1 - \varepsilon_2} \ln\left(\frac{N_1}{N_2}\right)\right), \quad \varepsilon_1 \leq \varepsilon \leq \varepsilon_2. \quad (\text{A6})$$

The stable pore radius r_p is now computed as the local minimum of the normalized membrane energy \hat{W}_N with respect to r_0 . With the closure (A6), analysis of Eq. (A1) shows that a local minimum at some $r_0^* > 0$ exists for all $\varepsilon \in [\varepsilon_1, \varepsilon_2]$. The position of this minimum can then be calculated analytically:

$$r_0^*(\varepsilon) = 2\sqrt{\frac{B(\varepsilon)}{6A(\varepsilon)N(\varepsilon)}} \cos\left(\frac{1}{3} \arccos\left(\frac{-3C(\varepsilon)}{4B(\varepsilon)} \sqrt{\frac{6A(\varepsilon)N(\varepsilon)}{B(\varepsilon)}}\right)\right).$$

Below ε_1 , no pores are forming. Above ε_2 , the membrane is considered to be fully ruptured. The pore radius r_p is thus given by:

$$r_p = \begin{cases} 0, & \varepsilon < \varepsilon_1, \\ r_0^*(\varepsilon), & \varepsilon_1 \leq \varepsilon \leq \varepsilon_2, \\ r_0^*(\varepsilon_2), & \varepsilon > \varepsilon_2. \end{cases} \quad (\text{A7})$$

Finally, the total pore area for a single RBC is given by:

$$A_p = \Phi_\varepsilon(\varepsilon) := \pi(1 + \varepsilon)A_0 N(\varepsilon) r_p^2(\varepsilon), \quad (\text{A8})$$

with the expressions from Eqs. (A6) and (A7). The function Φ_ε thus defines the pore area in terms of the surface strain ε . This has been the model as introduced by Vitale et al. [30].

Next, we derive a function

$$\varepsilon = \Psi_G(G_{\text{eff}}), \quad (\text{A9})$$

which will allow us to evaluate the surface strain ε for any of the models in Section 2.2. First, we determine the surface area of an arbitrary ellipsoid with semi-axes (a, b, c) . For this purpose, we use the convergent series by Keller [57]:

$$A_{\text{ell}}(a, b, c; n) = 2\pi bc + \frac{4\pi ab}{n} \sum_{j=1}^{n/2} \frac{1 - \tau_j}{\sqrt{1 - \left(\frac{c}{a}\right)^2 - \tau_j}} \arcsin \sqrt{\frac{1 - \left(\frac{c}{a}\right)^2 - \tau_j}{1 - \tau_j}},$$

$$\tau_j = \cos\left(\frac{(2j-1)\pi}{2n}\right), \quad \tau_j = \left(1 - \left(\frac{c}{b}\right)^2\right) t_j^2, \quad n \text{ even},$$

which converges to the true surface area of an ellipsoid as $n \rightarrow \infty$. In our computations, we use $n = 60$. For the TTM, we thus compute the surface area using the semi-axes obtained from Eq. (4a):

$$A_{\text{TTM}}(\boldsymbol{\Lambda}) = A_{\text{ell}}(\sqrt{\lambda_1}, \sqrt{\lambda_2}, \sqrt{\lambda_3}; 60). \quad (\text{A10})$$

At lethal hemolysis, real RBCs have 1.06 times the surface area of their resting state A_0 [40]. The ellipsoidal representation in the TTM leads to excess surface area in their resting state (sphere). As a result, lethal hemolysis in the ellipsoidal representation occurs at 1.4×1.06 times the original surface area A_s [40]. Assuming a linear relationship between the ellipsoidal surface strain in the TTM model and the surface strain of the RBC, we can thus relate the two as follows:

$$\varepsilon^{(2)} = \frac{1.06A_0 - A_0}{A_0}, \quad \varepsilon_{\text{TTM}}^{(2)} = \frac{1.4 \cdot 1.06A_s - A_s}{A_s}, \quad \varepsilon = \frac{\varepsilon^{(2)}}{\varepsilon_{\text{TTM}}^{(2)}} \varepsilon_{\text{TTM}} = \frac{15}{121} \varepsilon_{\text{TTM}}. \quad (\text{A11})$$

From Eqs. (A10) and (A11), we compute the surface strain for any deformation $\boldsymbol{\Lambda}$ as:

$$\varepsilon = \Psi_{\boldsymbol{\Lambda}}(\boldsymbol{\Lambda}) := \frac{A_{\text{TTM}}(\boldsymbol{\Lambda}) - A_s}{A_s} \cdot \frac{15}{121}, \quad A_s = 4\pi(\lambda_1 \lambda_2 \lambda_3)^{1/3}, \quad (\text{A12})$$

where A_s is the surface area of a sphere with the same volume as the ellipsoid defined by $\boldsymbol{\Lambda}$.

Finally, we need to find a way to determine the equivalent ellipsoidal shape $\boldsymbol{\Lambda}$ from the effective shear rate G_{eff} for the other RBC models discussed in Section 2.2. For

this purpose, we employ the steady state shear deformation values derived by Arora et al. [40]:

$$\begin{aligned}\lambda_1^{\text{steady}}(G) &= \left(\frac{f_1^2}{f_1^2 + f_2^2 G^2} \right)^{1/3} \frac{f_1^2 + f_2^2 G^2 + f_2 G \sqrt{f_1^2 + f_2^2 G^2}}{f_1^2}, \\ \lambda_2^{\text{steady}}(G) &= \left(\frac{f_1^2}{f_1^2 + f_2^2 G^2} \right)^{1/3}, \\ \lambda_3^{\text{steady}}(G) &= \left(\frac{f_1^2}{f_1^2 + f_2^2 G^2} \right)^{1/3} \frac{f_1^2 + f_2^2 G^2 - f_2 G \sqrt{f_1^2 + f_2^2 G^2}}{f_1^2}.\end{aligned}\quad (\text{A13})$$

These give the steady state deformation of an ellipsoidal RBC in simple shear flow with shear rate G . By evaluating these expressions at the effective shear rate G_{eff} provided by the RBC models, we obtain an estimate for the instantaneous equivalent ellipsoidal shape:

$$\boldsymbol{\Lambda}_{\text{eff}}(G_{\text{eff}}) = \mathbf{diag}(\lambda_1^{\text{steady}}(G_{\text{eff}}), \lambda_2^{\text{steady}}(G_{\text{eff}}), \lambda_3^{\text{steady}}(G_{\text{eff}})). \quad (\text{A14})$$

The surface strain can now be computed from Eqs. (A12) and (A14) as

$$\varepsilon = \Psi_G(G_{\text{eff}}) := \Psi_{\boldsymbol{\Lambda}}(\boldsymbol{\Lambda}_{\text{eff}}(G_{\text{eff}})). \quad (\text{A15})$$

This gives us the desired relation (A9) between the surface strain ε and the effective shear rate G_{eff} . We determine the threshold effective shear rate $G_{\text{eff}}^{(1)}$ and the lethal effective shear rate $G_{\text{eff}}^{(2)}$ such that

$$\Psi_G(G_{\text{eff}}^{(1)}) = \varepsilon_1, \quad \Psi_G(G_{\text{eff}}^{(2)}) = \varepsilon_2. \quad (\text{A16})$$

In the range between $G_{\text{eff}}^{(1)}$ and $G_{\text{eff}}^{(2)}$, we can thus evaluate the total pore area as a function of the effective shear rate by combining Eqs. (A8) and (A15):

$$A_p = \Phi_G(G_{\text{eff}}) := \Phi_{\varepsilon}(\Psi_G(G_{\text{eff}})) = \Phi_{\varepsilon}(\Psi_{\boldsymbol{\Lambda}}(\boldsymbol{\Lambda}_{\text{eff}}(G_{\text{eff}}))), \quad (\text{A17})$$

The resulting pore area A_p as a function of the effective shear rate G_{eff} is shown in Fig. A1. Finally, we evaluate Eq. (A17) for 10000 values of G_{eff} linearly spaced between $G_{\text{eff}}^{(1)}$ and $G_{\text{eff}}^{(2)}$ and fit a fifth-order polynomial P_5 to the resulting data using least squares minimization, i.e.,

$$P_5(G_{\text{eff}}/G_2) = \sum_{i=0}^5 a_i (G_{\text{eff}}/G_2)^i \approx \Phi_G(G_{\text{eff}}), \quad G_1 \leq G_{\text{eff}} \leq G_2. \quad (\text{A18})$$

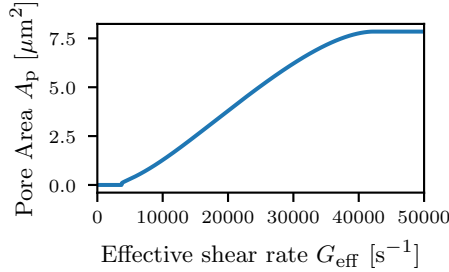


Fig. A1: Pore area A_p as a function of the effective shear rate G_{eff} .

We obtain a polynomial fit with a mean square error of $3.3124 \times 10^{-6} \mu\text{m}^4$. This yields the simplified expression for the pore area as a function of the effective shear rate:

$$P_5(x) = \sum_{i=0}^5 a_i x^i, \quad A_p(G_{\text{eff}}) = \begin{cases} 0, & G_{\text{eff}} < G_1, \\ P_5(G_{\text{eff}}/G_2), & G_1 \leq G_{\text{eff}} \leq G_2, \\ P_5(1), & G_{\text{eff}} > G_2. \end{cases}$$

References

- [1] Katz, J.N., Jensen, B.C., Chang, P.P., Myers, S.L., Pagani, F.D., Kirklin, J.K.: A Multicenter Analysis of Clinical Hemolysis in Patients Supported with Durable, Long-Term Left Ventricular Assist Device Therapy. *The Journal of Heart and Lung Transplantation* **34**(5), 701–709 (2015) <https://doi.org/10.1016/j.healun.2014.10.002>
- [2] Shah, P., Tantry, U.S., Bliden, K.P., Gurbel, P.A.: Bleeding and thrombosis associated with ventricular assist device therapy. *The Journal of Heart and Lung Transplantation* **36**(11), 1164–1173 (2017) <https://doi.org/10.1016/j.healun.2017.05.008>
- [3] Omar, H.R., Mirsaeidi, M., Socias, S., Sprenker, C., Caldeira, C., Camporesi, E.M., Mangar, D.: Plasma Free Hemoglobin Is an Independent Predictor of Mortality among Patients on Extracorporeal Membrane Oxygenation Support. *PLOS ONE* **10**(4), 0124034 (2015) <https://doi.org/10.1371/journal.pone.0124034>
- [4] Lyu, L., Long, C., Hei, F., Ji, B., Liu, J., Yu, K., Chen, L., Yao, J., Hu, Q., Hu, J., Gao, G.: Plasma Free Hemoglobin Is a Predictor of Acute Renal Failure During Adult Venous-Arterial Extracorporeal Membrane Oxygenation Support. *Journal of Cardiothoracic and Vascular Anesthesia* **30**(4), 891–895 (2016) <https://doi.org/10.1053/j.jvca.2016.02.011>

- [5] Ponnaluri, S.V., Hariharan, P., Herbertson, L.H., Manning, K.B., Malinauskas, R.A., Craven, B.A.: Results of the Interlaboratory Computational Fluid Dynamics Study of the FDA Benchmark Blood Pump. *Annals of Biomedical Engineering* **51**(1), 253–269 (2023) <https://doi.org/10.1007/s10439-022-03105-w>
- [6] Ezzeldin, H.M., de Tullio, M.D., Vanella, M., Solares, S.D., Balaras, E.: A Strain-Based Model for Mechanical Hemolysis Based on a Coarse-Grained Red Blood Cell Model. *Annals of Biomedical Engineering* **43**(6), 1398–1409 (2015) <https://doi.org/10.1007/s10439-015-1273-z>
- [7] Závodszky, G., van Rooij, B., Azizi, V., Hoekstra, A.: Cellular Level In-Silico Modeling of Blood Rheology with an Improved Material Model for Red Blood Cells. *Frontiers in Physiology* **8** (2017) <https://doi.org/10.3389/fphys.2017.00563>
- [8] Mendez, S., Gibaud, E., Nicoud, F.: An unstructured solver for simulations of deformable particles in flows at arbitrary Reynolds numbers. *Journal of Computational Physics* **256**, 465–483 (2014) <https://doi.org/10.1016/j.jcp.2013.08.061>
- [9] Fedosov, D.A., Caswell, B., Karniadakis, G.E.: A Multiscale Red Blood Cell Model with Accurate Mechanics, Rheology, and Dynamics. *Biophysical Journal* **98**(10), 2215–2225 (2010) <https://doi.org/10.1016/j.bpj.2010.02.002>
- [10] Guglietta, F., Behr, M., Falcucci, G., Sbragaglia, M.: Loading and Relaxation Dynamics of a Red Blood Cell. *Soft Matter* **17**, 5978–5990 (2021) <https://doi.org/10.1039/D1SM00246E>
- [11] Puig-de-Morales-Marinkovic, M., Turner, K.T., Butler, J.P., Fredberg, J.J., Suresh, S.: Viscoelasticity of the Human Red Blood Cell. *American Journal of Physiology-Cell Physiology* **293**(2), 597–605 (2007) <https://doi.org/10.1152/ajpcell.00562.2006>
- [12] Hochmuth, R.M., Worthy, P.R., Evans, E.A.: Red cell extensional recovery and the determination of membrane viscosity. *Biophysical Journal* **26**(1), 101–114 (1979) [https://doi.org/10.1016/S0006-3495\(79\)85238-8](https://doi.org/10.1016/S0006-3495(79)85238-8)
- [13] Katchalsky, A., Kedem, O., Klibansky, C., De Vries, A.: Rheological considerations of the haemolysing red blood cell. In: *Flow Properties of Blood and Other Biological Systems*, pp. 155–171. Pergamon Press Inc., New York (1960)
- [14] Rand, R.P.: Mechanical Properties of the Red Cell Membrane: II. Viscoelastic Breakdown of the Membrane. *Biophysical Journal* **4**(4), 303–316 (1964) [https://doi.org/10.1016/S0006-3495\(64\)86784-9](https://doi.org/10.1016/S0006-3495(64)86784-9)
- [15] Lommel, M., Froese, V., Wolff, H., Dirkes, N., Vellguth, K., Behr, M., Kertzscher, U.: Experimental Investigation of the Applicability of the Stress-Based and Strain-Based Hemolysis Models for Short-Term Stress Peaks Typical for Rotatory

Blood Pumps. Artificial Organs **49**(7), 1108–1118 <https://doi.org/10.1111/aor.15002>

- [16] Arwatz, G., Smits, A.J.: A Viscoelastic Model of Shear-Induced Hemolysis in Laminar Flow. *Biorheology* **50**(1-2), 45–55 (2013) <https://doi.org/10.3233/BIR-130626>
- [17] Chen, Y., Sharp, M.K.: A Strain-Based Flow-Induced Hemolysis Prediction Model Calibrated by In Vitro Erythrocyte Deformation Measurements. *Artificial Organs* **35**(2), 145–156 (2011) <https://doi.org/10.1111/j.1525-1594.2010.01050.x>
- [18] Yeleswarapu, K.K., Antaki, J.F., Kameneva, M.V., Rajagopal, K.R.: A Mathematical Model for Shear-Induced Hemolysis. *Artificial Organs* **19**(7), 576–582 (1995) <https://doi.org/10.1111/j.1525-1594.1995.tb02384.x>
- [19] Chen, Y., Kent, T.L., Sharp, M.K.: Testing of Models of Flow-Induced Hemolysis in Blood Flow Through Hypodermic Needles. *Artificial Organs* **37**(3), 256–266 (2013) <https://doi.org/10.1111/j.1525-1594.2012.01569.x>
- [20] Lee, S., Cho, Y., Kang, S., Hur, N., Kim, W.: Evaluation of an extended viscoelastic model to predict hemolysis in cannulas and blood pumps. *Journal of Mechanical Science and Technology* **33**(5), 2181–2188 (2019) <https://doi.org/10.1007/s12206-019-0420-0>
- [21] Yu, H., Engel, S., Janiga, G., Thévenin, D.: A Review of Hemolysis Prediction Models for Computational Fluid Dynamics. *Artificial Organs* **41**(7), 603–621 (2017) <https://doi.org/10.1111/aor.12871>
- [22] Dirkes, N., Key, F., Behr, M.: Eulerian formulation of the tensor-based morphology equations for strain-based blood damage modeling. *Computer Methods in Applied Mechanics and Engineering* **426**, 116979 (2024) <https://doi.org/10.1016/j.cma.2024.116979>
- [23] Dirkes, N., Behr, M.: On the significance of flow vorticity for hemolysis modeling. In: *Topical Problems of Fluid Mechanics*, pp. 51–58. Institute of Thermomechanics of the Czech Academy of Sciences; CTU in Prague Faculty of Mech. Engineering Dept. Tech. Mathematics, Prague, Czechia (2025). <https://doi.org/10.14311/TPFM.2025.008>
- [24] Faghah, M.M., Sharp, M.K.: Deformation of Human Red Blood Cells in Extensional Flow through a Hyperbolic Contraction. *Biomechanics and Modeling in Mechanobiology* **19**(1), 251–261 (2020) <https://doi.org/10.1007/s10237-019-01208-3>
- [25] Faghah, M.M., Sharp, M.K.: Modeling and prediction of flow-induced hemolysis: A review. *Biomechanics and Modeling in Mechanobiology* **18**(4), 845–881 (2019) <https://doi.org/10.1007/s10237-019-01137-1>

[26] Poorkhalil, A., Amoabediny, G., Tabesh, H., Behbahani, M., Mottaghay, K.: A New Approach for Semiempirical Modeling of Mechanical Blood Trauma. *The International Journal of Artificial Organs* **39**(4), 171–177 (2016) <https://doi.org/10.5301/ijao.5000474>

[27] McKean, A.: Development of a Hemolysis Model with Sublethal Hemoglobin Release. Master's thesis, McGill University (2020)

[28] Giersiepen, M., Wurzinger, L.J., Opitz, R., Reul, H.: Estimation of Shear Stress-Related Blood Damage in Heart Valve Prostheses—In Vitro Comparison of 25 Aortic Valves. *International Journal of Artificial Organs* **13**(5), 300–306 (1990) <https://doi.org/10.1177/039139889001300507>

[29] Ding, J., Niu, S., Chen, Z., Zhang, T., Griffith, B.P., Wu, Z.J.: Shear-Induced Hemolysis: Species Differences. *Artificial Organs* **39**(9), 795–802 (2015) <https://doi.org/10.1111/aor.12459>

[30] Vitale, F., Nam, J., Turchetti, L., Behr, M., Raphael, R., Annesini, M.C., Pasquali, M.: A multiscale, biophysical model of flow-induced red blood cell damage. *AIChE Journal* **60**(4), 1509–1516 (2014) <https://doi.org/10.1002/aic.14318>

[31] Sohrabi, S., Liu, Y.: A Cellular Model of Shear-Induced Hemolysis. *Artificial Organs* **41**(9), 80–91 (2017) <https://doi.org/10.1111/aor.12832>

[32] Haßler, S., Ranno, A.M., Behr, M.: Finite-element formulation for advection-reaction equations with change of variable and discontinuity capturing. *Computer Methods in Applied Mechanics and Engineering* **369**, 113171 (2020) <https://doi.org/10.1016/j.cma.2020.113171>

[33] Pauli, L.: Stabilized Finite Element Methods for Computational Design of Blood-Handling Devices. PhD thesis, RWTH Aachen University, Aachen, Germany (2016)

[34] Melka, B., Adamczyk, W.P., Rojczyk, M., Nowak, M.L., Gracka, M., Nowak, A.J., Golda, A., Bialecki, R.A., Ostrowski, Z.: Numerical investigation of multi-phase blood flow coupled with lumped parameter model of outflow. *International Journal of Numerical Methods for Heat & Fluid Flow* **30**(1), 228–244 (2019) <https://doi.org/10.1108/HFF-04-2019-0279>

[35] Bodnár, T., Rajagopal, K.R., Sequeira, A.: Simulation of the Three-Dimensional Flow of Blood Using a Shear-Thinning Viscoelastic Fluid Model. *Mathematical Modelling of Natural Phenomena* **6**(5), 1–24 (2011) <https://doi.org/10.1051/mmnp/20116501>

[36] Krisher, J.A., Malinauskas, R.A., Day, S.W.: The effect of blood viscosity on shear-induced hemolysis using a magnetically levitated shearing device. *Artificial*

Organs **46**(6), 1027–1039 (2022) <https://doi.org/10.1111/aor.14172>

[37] Bludszuweit, C.: Model for a General Mechanical Blood Damage Prediction. *Artificial Organs* **19**(7), 583–589 (1995) <https://doi.org/10.1111/j.1525-1594.1995.tb02385.x>

[38] Hénon, S., Lenormand, G., Richert, A., Gallet, F.: A New Determination of the Shear Modulus of the Human Erythrocyte Membrane Using Optical Tweezers. *Biophysical Journal* **76**(2), 1145–1151 (1999) [https://doi.org/10.1016/S0006-3495\(99\)77279-6](https://doi.org/10.1016/S0006-3495(99)77279-6)

[39] Bronkhorst, P.J., Streekstra, G.J., Grimbergen, J., Nijhof, E.J., Sixma, J.J., Brakenhoff, G.J.: A new method to study shape recovery of red blood cells using multiple optical trapping. *Biophysical Journal* **69**(5), 1666–1673 (1995) [https://doi.org/10.1016/S0006-3495\(95\)80084-6](https://doi.org/10.1016/S0006-3495(95)80084-6)

[40] Arora, D., Behr, M., Pasquali, M.: A Tensor-Based Measure for Estimating Blood Damage. *Artificial Organs* **28**(11), 1002–1015 (2004) <https://doi.org/10.1111/j.1525-1594.2004.00072.x>

[41] Haßler, S., Pauli, L., Behr, M.: The Variational Multiscale Formulation for the Fully-Implicit Log-Morphology Equation as a Tensor-Based Blood Damage Model. *International Journal for Numerical Methods in Biomedical Engineering* **35**(12), 3262 (2019) <https://doi.org/10.1002/cnm.3262>

[42] Taskin, M.E., Fraser, K.H., Zhang, T., Wu, C., Griffith, B.P., Wu, Z.J.: Evaluation of Eulerian and Lagrangian models for hemolysis estimation. *ASAIO journal (American Society for Artificial Internal Organs)* **58**(4), 363–372 (2012) <https://doi.org/10.1097/MAT.0b013e318254833b>

[43] Blum, C., Mous, M., Steinseifer, U., Claußer, J.C., Neidlin, M.: Quantifying Experimental Variability in Shear-Induced Hemolysis to Support Uncertainty-Aware Hemolysis Models. *Annals of Biomedical Engineering* **53**(10), 2551–2561 (2025) <https://doi.org/10.1007/s10439-025-03786-z>

[44] Faghih, M.M., Craven, B.A., Sharp, M.K.: Practical implications of the erroneous treatment of exposure time in the Eulerian hemolysis power law model. *Artificial Organs* **47**(9), 1531–1538 (2023) <https://doi.org/10.1111/aor.14543>

[45] Lacasse, D., Garon, A., Pelletier, D.: Mechanical hemolysis in blood flow: User-independent predictions with the solution of a partial differential equation. *Computer Methods in Biomechanics and Biomedical Engineering* **10**(1), 1–12 (2007) <https://doi.org/10.1080/10255840600985535>

[46] Craven, B.A., Aycock, K.I., Herbertson, L.H., Malinauskas, R.A.: A CFD-based Kriging surrogate modeling approach for predicting device-specific hemolysis power law coefficients in blood-contacting medical devices. *Biomechanics and*

Modeling in Mechanobiology **18**(4), 1005–1030 (2019) <https://doi.org/10.1007/s10237-019-01126-4>

- [47] Garon, A., Farinas, M.-I.: Fast three-dimensional numerical hemolysis approximation. *Artificial Organs* **28**(11), 1016–1025 (2004) <https://doi.org/10.1111/j.1525-1594.2004.00026.x>
- [48] Pauli, L., Both, J., Behr, M.: Stabilized Finite Element Method for Flows with Multiple Reference Frames. *International Journal for Numerical Methods in Fluids* **78**(11), 657–669 (2015) <https://doi.org/10.1002/fld.4032>
- [49] Bazilevs, Y., Calo, V.M., Cottrell, J.A., Hughes, T.J.R., Reali, A., Scovazzi, G.: Variational multiscale residual-based turbulence modeling for large eddy simulation of incompressible flows. *Computer Methods in Applied Mechanics and Engineering* **197**(1), 173–201 (2007) <https://doi.org/10.1016/j.cma.2007.07.016>
- [50] Malinauskas, R.A., Hariharan, P., Day, S.W., Herbertson, L.H., Buesen, M., Steinseifer, U., Aycock, K.I., Good, B.C., Deutsch, S., Manning, K.B., Craven, B.A.: FDA Benchmark Medical Device Flow Models for CFD Validation. *ASAIO Journal* **63**(2), 150 <https://doi.org/10.1097/MAT.0000000000000499>
- [51] Hariharan, P., Giarra, M., Reddy, V., Day, S.W., Manning, K.B., Deutsch, S., Stewart, S.F.C., Myers, M.R., Berman, M.R., Burgreen, G.W., Paterson, E.G., Malinauskas, R.A.: Multilaboratory Particle Image Velocimetry Analysis of the FDA Benchmark Nozzle Model to Support Validation of Computational Fluid Dynamics Simulations. *Journal of Biomechanical Engineering* **133**(041002) (2011) <https://doi.org/10.1115/1.4003440>
- [52] Mantegazza, A., Tobin, N., Manning, K.B., Craven, B.A.: Examining the universality of the hemolysis power law model from simulations of the FDA nozzle using calibrated model coefficients. *Biomechanics and Modeling in Mechanobiology* **22**(2), 433–451 (2023) <https://doi.org/10.1007/s10237-022-01655-5>
- [53] Herbertson, L.H., Olia, S.E., Daly, A., Noatch, C.P., Smith, W.A., Kameneva, M.V., Malinauskas, R.A.: Multilaboratory Study of Flow-Induced Hemolysis Using the FDA Benchmark Nozzle Model. *Artificial Organs* **39**(3), 237–248 (2015) <https://doi.org/10.1111/aor.12368>
- [54] Goubergrits, L., Osman, J., Mevert, R., Kertzscher, U., Pöthkow, K., Hege, H.-C.: Turbulence in Blood Damage Modeling. *The International Journal of Artificial Organs* **39**(4), 160–165 (2016) <https://doi.org/10.5301/ijao.5000476>
- [55] Wu, P., Gao, Q., Hsu, P.-L.: On the representation of effective stress for computing hemolysis. *Biomechanics and Modeling in Mechanobiology* **18**(3), 665–679 (2019) <https://doi.org/10.1007/s10237-018-01108-y>
- [56] Blum, C., Steinseifer, U., Neidlin, M.: Toward Uncertainty-Aware Hemolysis

Modeling: A Universal Approach to Address Experimental Variance. International Journal for Numerical Methods in Biomedical Engineering **41**(5), 70040 (2025) <https://doi.org/10.1002/cnm.70040>

[57] Keller, S.R.: On the Surface Area of the Ellipsoid. Mathematics of Computation **33**(145), 310–314 (1979) <https://doi.org/10.2307/2006043>